

# The phononic and charge density wave behavior of entire rare-earth tritelluride series with chemical pressure and temperature

Cite as: APL Mater. 10, 111112 (2022); <https://doi.org/10.1063/5.0110395>

Submitted: 15 July 2022 • Accepted: 11 October 2022 • Published Online: 11 November 2022

Kentaro Yumigeta, Yashika Attarde, Jan Kopaczek, et al.



View Online



Export Citation



CrossMark

## ARTICLES YOU MAY BE INTERESTED IN

[Metal-insulator transitions in dimensionality controlled  \$\text{La}\_x\text{Sr}\_{1-x}\text{VO}\_3\$  films](#)

APL Materials 10, 111114 (2022); <https://doi.org/10.1063/5.0122864>

[Magnetic hopfions in solids](#)

APL Materials 10, 111113 (2022); <https://doi.org/10.1063/5.0099942>

[Raman spectra and dimensional effect on the charge density wave transition in  \$\text{GdTe}\_3\$](#)

Applied Physics Letters 115, 151905 (2019); <https://doi.org/10.1063/1.5118870>



## APL Machine Learning

Machine Learning for Applied Physics  
Applied Physics for Machine Learning

**First Articles  
Now Online!**

# The phononic and charge density wave behavior of entire rare-earth tritelluride series with chemical pressure and temperature

Cite as: APL Mater. 10, 111112 (2022); doi: 10.1063/5.0110395

Submitted: 15 July 2022 • Accepted: 11 October 2022 •

Published Online: 11 November 2022



View Online



Export Citation



CrossMark

Kentaro Yumigeta, Yashika Attarde, Jan Kopaczek, Mohammed Y. Sayyad, Yuxia Shen, Mark Blei, Seyed Tohid Rajaei Moosavy, Ying Qin, Renee Sailus, and Sefaattin Tongay<sup>a)</sup>

## AFFILIATIONS

School for Engineering of Matter, Transport and Energy, Arizona State University, Tempe, Arizona 85287, USA

<sup>a)</sup> Author to whom correspondence should be addressed: [Sefaattin.tongay@asu.edu](mailto:Sefaattin.tongay@asu.edu)

## ABSTRACT

Here, we present comprehensive phononic and charge density wave properties (CDW) of rare-earth van der Waals tritellurides through temperature dependent angle-resolved Raman spectroscopy measurements. All the possible rare-earth tritellurides ( $\text{RTe}_3$ ) ranging from  $\text{R} = \text{La-Nd, Sm, Gd-Tm}$  were synthesized through a chemical vapor transport technique to achieve high quality crystals with excellent CDW characteristics. Raman spectroscopy studies successfully identify the emergence of the CDW state and transition temperature ( $T_{\text{CDW}}$ ), which offers a non-destructive method to identify their CDW response with micron spatial resolution. Temperature dependent Raman measurements further correlate how the atomic mass of metal cations and the resulting chemical pressure influence its CDW properties and offer detailed insight into the strength of CDW amplitude mode-phonon coupling during the CDW transition. Angle-resolved Raman measurements offer the first insights into the CDW-phonon symmetry interplay by monitoring the change in the symmetry of phonon mode across the CDW transition. Overall results introduce the library of  $\text{RTe}_3$  CDW materials and establish their characteristics through the non-destructive angle-resolved Raman spectroscopy technique.

© 2022 Author(s). All article content, except where otherwise noted, is licensed under a Creative Commons Attribution (CC BY) license (<http://creativecommons.org/licenses/by/4.0/>). <https://doi.org/10.1063/5.0110395>

## INTRODUCTION

Rare-earth tritellurides ( $\text{RTe}_3$ ,  $\text{R} = \text{La-Nd, Sm, Gd-Tm}$ ) is a family of antiferromagnetic layered materials wherein individual  $\text{RTe}_3$  sheets are coupled to each other through weak van der Waals (vdW) interactions. Recently, rare earth tritellurides have attracted much attention owing to their high electron mobility in the magnetically ordered vdW materials,<sup>1</sup> the presence of superconductivity under high pressure and intercalation,<sup>2,3</sup> and other emergent quantum properties and effects.<sup>4-14</sup>  $\text{RTe}_3$  sheets consist of two tellurium layers separated by an RTe slab in the unit cell as shown in Fig. 1(a).  $\text{RTe}_3$  has an orthorhombic crystal structure with a slight in-plane anisotropy ( $a \sim 0.999c$ ), which results in a preferred charge density wave (CDW) order direction along the  $c$ -axis [Fig. 1(a)]. The lattice parameter varies with the R lanthanide atom's Bohr radius and leads to an effective chemical pressure that affects the transition temperature of CDW states.<sup>15-17</sup> All  $\text{RTe}_3$  show a unidirectional

incommensurate CDW state with the wavevector  $q_c = (0, 0, \sim 2/7 c^*)$  at the transition temperature ranging from 250 K in  $\text{TmTe}_3$  to 540 K in  $\text{CeTe}_3$ , and an even higher temperature is expected in  $\text{LaTe}_3$ .<sup>13,18,19</sup> For heavy R elements (Tb-Tm), a second incommensurate CDW state with the wavevector  $q_c = (\sim 2/7 a^*, 0, 0)$  occurs perpendicular to the first CDW wavevector  $q_c$  at the temperature ranging from 41 K in  $\text{TbTe}_3$  to 186 K in  $\text{TmTe}_3$ .<sup>18,20,21</sup>

Usually, measurements are carried out using electrical transport studies after  $\text{RTe}_3$  sheets undergo heavy microfabrication steps, and the measured response is an average over a large area. Due to the poor environmental stability of some of these rare-earth tritelluride materials, they can quickly oxidize or can even become defective after processing, resulting in a change of physical properties. Limited optical spectroscopy studies suggested the emergence of CDW phase transition of selected  $\text{RTe}_3$  containing La, Gd, Dy, or Er.<sup>22-25</sup> More comprehensive studies across the entire  $\text{RTe}_3$  family

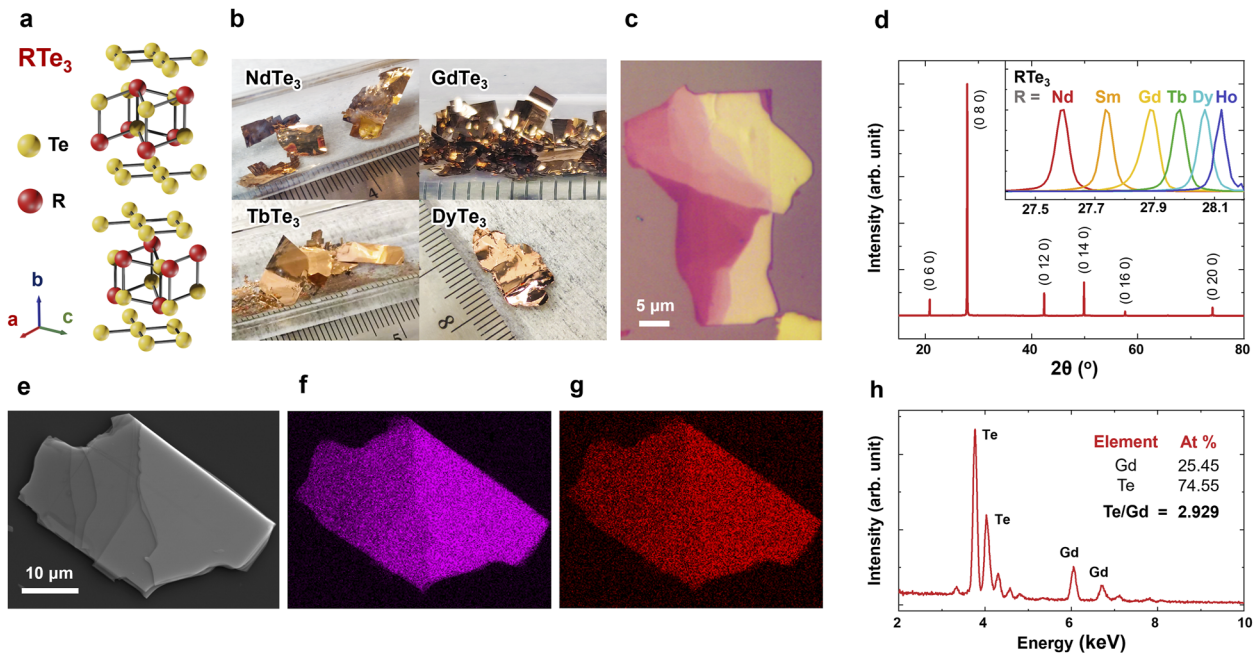


**FIG. 1.** (a) The crystal structure of rare-earth tritellurides. (b) The optical images of  $R\text{Te}_3$  crystals. (c) The optical image of an exfoliated  $\text{GdTe}_3$  sheet on a  $\text{SiO}_2/\text{Si}$  substrate. (d) X-ray diffraction spectrum from a  $\text{GdTe}_3$  single crystal. The inset shows the (0 8 0) reflection of the series of  $R\text{Te}_3$  crystals ranging from  $R = \text{Nd}, \text{Sm}, \text{Gd}-\text{Tm}$ . (e) Scanning electron microscopy (SEM) image and energy-dispersive x-ray spectroscopy (EDS) elemental mapping results of (f) Te and (g) Gd for  $\text{GdTe}_3$  exfoliated sheets. (h) EDS spectrum of  $\text{GdTe}_3$ .

are needed to understand how the metal cation type and chemical pressure influence their CDW response and how CDW formation influences the phonon symmetry (angle-resolved Raman) across the CDW transition.

Here, we report on the comprehensive vibrational and charge density wave properties of the library of rare-earth tritellurides materials through cryogenic Raman spectroscopy and angle-resolved Raman spectroscopy. Using the chemical vapor transport (CVT) technique, all the possible rare-earth tritellurides ( $R\text{Te}_3$ ) were synthesized to include  $R = \text{La}-\text{Nd}, \text{Sm}, \text{Gd}-\text{Tm}$ . Through systematic Raman spectroscopy studies, the emergent CDW vibrational fingerprints were identified for a given lanthanide metal cation by monitoring the changes in the Raman spectra as the temperature was swept and the material underwent the CDW transition. Furthermore, decreasing the Bohr radius of rare-earth metal cations going from  $R = \text{La}$  to  $\text{Tm}$  allowed us to correlate the CDW properties to increasing chemical pressure through micron resolution cryogenic Raman spectroscopy. For the first time, angle-resolved Raman spectroscopy on  $R\text{Te}_3$  sheets was performed, which revealed large changes in the Raman polar plots across the CDW transition temperature associated with the Raman tensor changes triggered by the onset of the CDW phase.

**The CVT synthesis of rare-earth tritelluride crystals.**  $R\text{Te}_3$  crystals were synthesized by chemical vapor transport (CVT) to yield large  $R\text{Te}_3$  crystals as shown in Fig. 1(b). One gram of a stoichiometric mixture of rare-earth metal (99.9%, Alfa Aesar) and tellurium (99.999%, Alfa Aesar) was sealed with a transport agent in a quartz

ampoule under a vacuum of  $10^{-5}$  Torr. In a typical growth, 20 mg of iodine ( $\text{I}_2$ ) for  $R = \text{La}-\text{Dy}$  and 40 mg of  $\text{TeCl}_4$  for  $R = \text{Ho}-\text{Tm}$  were used as a transport agent. The ampoule was heated at the rate of 2 K/min to the growth temperature ranging from 500 to 730 °C depending on which  $R\text{Te}_3$  is being grown (see the summary of growth parameters in [supplementary material](#) Table I). The growth process was carried out for 1 week, and subsequently, the temperature was controllably reduced to room temperature. The quartz ampoule was opened in a glovebox, and the crystals were stored in an inert environment to avoid degradation. The crystals were freshly exfoliated onto  $\text{SiO}_2/\text{Si}$  substrates using the standard mechanical exfoliation technique [Fig. 1(c)]. Because of the vdW interaction between two adjacent Te layers, the crystal can be easily exfoliated into thin and smooth films. Typical  $R\text{Te}_3$  exfoliated sheets measured  $\sim 100$  nm to microns in thickness. The crystal structure was characterized by x-ray diffraction (XRD) using Malvern PANalytical Aeris with  $\text{Cu K}\alpha$  radiation. The x-ray diffraction spectra of synthesized  $R\text{Te}_3$  crystals exhibited well-defined (0  $l$  0) reflections along the vdW stacking  $b$ -axis lattice direction with  $l = 2, 4, 6$ , and so on, as shown in Fig. 1(d), which was consistent with values reported in literature.<sup>26</sup> It is known that the atomic radius of lanthanides shrinks as the atomic number increases due to the poor shielding effect of 4f electrons, which is called lanthanide contraction. The lanthanide contraction results in a decreased lattice parameter for  $R\text{Te}_3$  crystals with heavier rare-earth elements.<sup>17</sup> Scanning electron microscopy (SEM) and energy-dispersive x-ray spectroscopy (EDS) measurements were performed using a JEOL JXA-8530F field

emission electron microprobe analyzer with an acceleration voltage of 20 kV. The SEM image shown in Fig. 1(e) also showed the layered nature of the synthesized  $\text{RTe}_3$  vdW crystals, and the EDS mappings have shown uniform rare-earth cation and chalcogen anion distribution across the entire flake as shown for  $\text{GdTe}_3$  in Figs. 1(f) and 1(g) with a 1:3 stoichiometric ratio of R to Te.

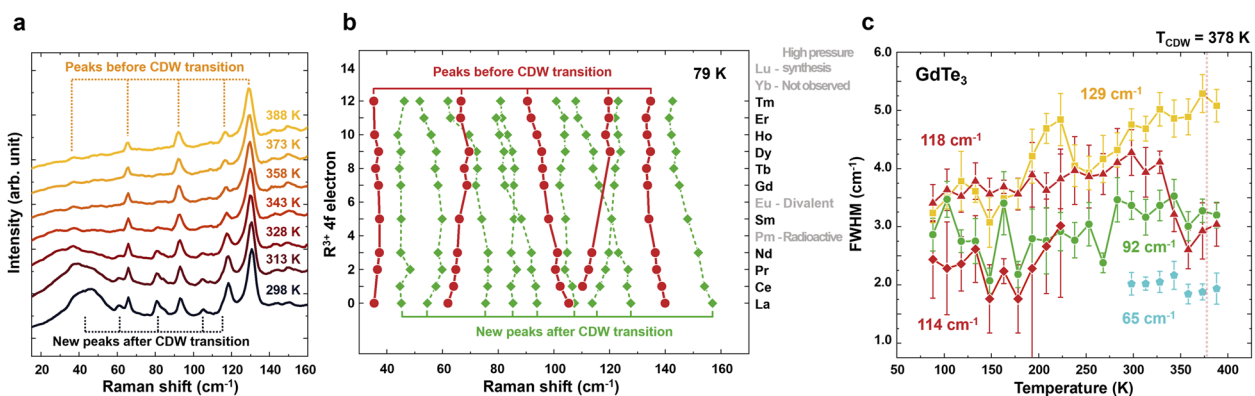
**Chemical pressure effects on the Vibrational characteristics.** To understand the effect of chemical pressure on the CDW and phononic properties of  $\text{RTe}_3$  crystals, temperature dependent Raman measurements were performed on exfoliated and bulk crystals using a 532 nm laser with a  $50\times$  objective lens. The laser spot size was kept the same ( $\sim 1 \mu\text{m}$ ) for all samples, and the laser power was set below  $750 \mu\text{W}$  to prevent sample degradation. Angle-resolved Raman spectroscopy (ARRS) measurements were also performed using the same setup. The scattered light was polarized parallel to the incident laser, and the polarization direction was rotated to collect Raman spectra at different angles, as demonstrated previously for other material systems.<sup>27–38</sup>

The temperature dependent Raman spectra of  $\text{GdTe}_3$  from 298 to 388 K are shown in Fig. 2(a). The broad shoulder located around  $\omega \leq 60 \text{ cm}^{-1}$  at 298 K shifts to lower frequencies (softens) as the temperature is increased. The peak eventually vanishes above the CDW transition temperature ( $T_{\text{CDW}} \sim 378 \text{ K}$ ) when the CDW order is thermally disturbed. This significant temperature dependence of the frequency is specific for a CDW amplitude mode.<sup>22,23,25,39–42</sup> Other small peaks at 60, 80, and  $110 \text{ cm}^{-1}$  lose their Raman intensity and eventually disappear above  $T_{\text{CDW}}$  without substantial frequency shifts, which indicates that these peaks originate from the CDW zone-folded modes due to the new lattice periodicity. The emergence of these new Raman peaks in the CDW state has been reported in various materials. The emergence of these new Raman peaks in the CDW state has been reported in various materials.<sup>22,24,25,39–41</sup> In contrast, the peaks at 65, 92, 118, and  $129 \text{ cm}^{-1}$  remain even above  $T_{\text{CDW}}$ , implying that they are related to the undistorted-state phonon modes.

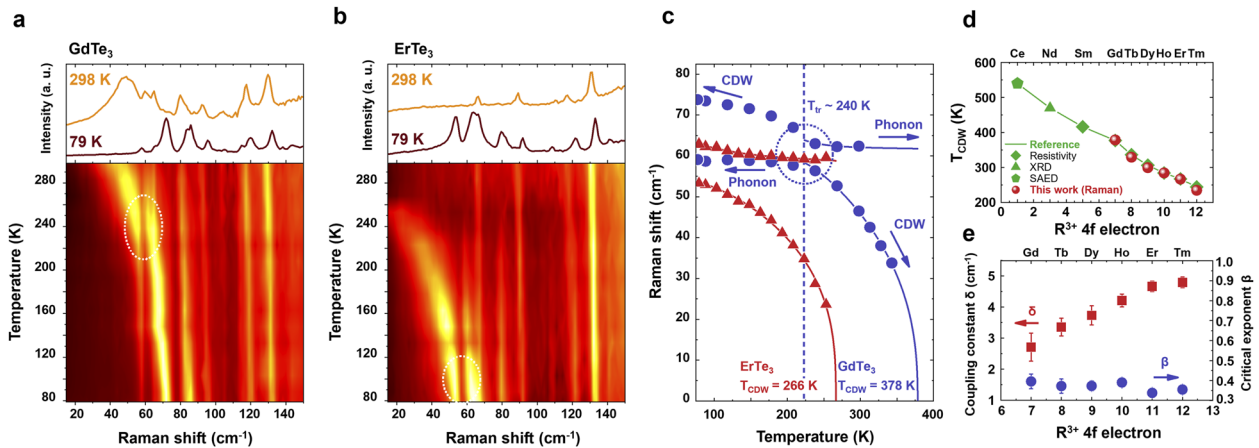
The Raman peak positions of other  $\text{RTe}_3$  materials with  $\text{R} = \text{La}–\text{Nd}, \text{Sm}, \text{Gd}–\text{Tm}$  were collected at 79 K and summarized in Fig. 2(b). As discussed above, the origin of Raman peaks is determined by temperature dependent Raman spectroscopy (the Raman spectra of the  $\text{RTe}_3$  series are shown in the supplementary material). The red circles represent the phonon peaks, and the green diamonds represent the CDW peaks. The peaks of the phonon modes at 35 and  $135 \text{ cm}^{-1}$  are independent of the rare-earth cation while the peak around  $100 \text{ cm}^{-1}$  softens, and the peaks around 60 and  $115 \text{ cm}^{-1}$  harden with the heavier rare-earth cations. Although the proximity of Raman peaks makes it difficult to deconvolute some of them, the trend of peak positions by a systematic study of Raman spectra through lanthanide series enables us to determine the peak positions.

Figure 2(c) shows the plot of full width at half maximum (FWHM) of phonon modes of  $\text{GdTe}_3$  shown in Fig. 2(a) as a function of temperature. The FWHM of the peaks decreased as the temperature decreased due to phonon anharmonicity. The peak at  $118 \text{ cm}^{-1}$  showed an anomalous increase of FWHM below  $T_{\text{CDW}}$ . This behavior was not observed in the other phonon modes. This broadening below  $T_{\text{CDW}}$  can be attributed to the emergence of new CDW peaks. As shown in Fig. 2(b), one phonon mode and two CDW modes exist around  $120 \text{ cm}^{-1}$ . The fact that the peak around  $120 \text{ cm}^{-1}$  splits into two peaks at low temperature [Fig. 3(a)] and supports the origin of the increase in FWHM.

Figures 3(a) and 3(b) show the Raman spectra collected from  $\text{GdTe}_3$  and  $\text{ErTe}_3$  from room temperature (300 K) down to 77 K. As the temperature decreased, the CDW amplitude mode frequency  $\omega_{\text{CDW}}$  appeared at  $\sim 360 \text{ K}$  for  $\text{GdTe}_3$  and at  $\sim 250 \text{ K}$  for  $\text{ErTe}_3$ , which is consistent with resistivity measurements as summarized in Fig. 3(d).<sup>22,23,25</sup> At low temperatures, the intensity of the CDW amplitude mode decreases, and the Raman shift becomes independent of temperature, while the intensity of the peak around  $60 \text{ cm}^{-1}$  becomes stronger and blueshifts at lower temperatures. This anti-crossing behavior is due to the interaction of the CDW amplitude mode and phonon mode and is consistent with prior works.<sup>22,23,42</sup>



**FIG. 2.** (a) Temperature-dependent Raman spectroscopy for  $\text{GdTe}_3$ . The signature CDW Raman mode is observed at  $\sim 50 \text{ cm}^{-1}$  as the temperature is lowered across the CDW transition temperature,  $T_{\text{CDW}}$ . (b) Identified Raman peaks for the entire lanthanide tritelluride series at  $T = 79 \text{ K}$ . Circles represent phonon modes related to the undistorted state. Diamonds represent peaks related to the CDW state. (c) FWHM of  $\text{GdTe}_3$  phonon modes. The major four phonon modes at  $65 \text{ cm}^{-1}$  (pentagons),  $92 \text{ cm}^{-1}$  (circles),  $118 \text{ cm}^{-1}$  (triangles), and  $129 \text{ cm}^{-1}$  (squares) are shown. At low temperatures, the  $118 \text{ cm}^{-1}$  mode splits into two peaks (triangles and diamonds). The 35 and  $65 \text{ cm}^{-1}$  modes at low temperatures are not shown due to the difficulty of deconvolution of these peaks related to phonon and CDW amplitude modes.



**FIG. 3.** Temperature dependent low-frequency Raman spectra of (a) GdTe<sub>3</sub> and (b) ErTe<sub>3</sub>. The dotted circles indicate the critical temperature  $T_{tr}$  where the peak intensities of CDW and phonon modes become comparable ( $T_{tr} = 240$  K for GdTe<sub>3</sub>, 90 K for ErTe<sub>3</sub>). (c) Temperature dependence of the CDW amplitude mode. The red and blue solid lines show the fittings based on the coupling of the phonon mode and the amplitude mode following the Ginzburg–Landau temperature dependence. The fitting is performed using the data points at temperatures above  $T_{tr}$ . (d) RTe<sub>3</sub> CDW transition temperature as a function of the rare-earth cations measured with various methods. The red spheres represent the transition temperatures estimated by the fitting on the peak position of the amplitude mode and phonon. The green symbols are determined by Resistivity measurement,<sup>15</sup> XRD,<sup>17</sup> and SAED.<sup>13</sup> (e) The coupling constant of the CDW amplitude mode and phonon mode (square), and  $\beta$  for Ginzburg–Landau temperature dependence (circle).

The intensities of the CDW peak and the phonon peak become comparable around the critical temperature  $T_{tr}$  as shown in Fig. 3(c) (blue dotted circles), and the peak around  $60\text{ cm}^{-1}$  starts to behave as a CDW amplitude mode above the critical temperature  $T_{tr}$ .

Here, the temperature dependence of the CDW mode ( $\omega_{CDW}$ ) can be described by the Ginzburg–Landau model in the form of  $\omega_{CDW} = \omega_0 \times \left(1 - \frac{T}{T_{CDW}}\right)^\beta$ .<sup>22,23,43</sup>  $\omega_{CDW}$  is the frequency of the CDW mode,  $\omega_0$  is the frequency of the CDW amplitude mode at low temperature, and the parameter  $\beta$  is a critical exponent. The CDW amplitude mode and the phonon mode  $\omega_{ph}$  interact through a coupling constant  $\delta$ . The interaction can be described by a matrix  $\begin{pmatrix} \omega_{CDW} & \delta \\ \delta & \omega_{ph} \end{pmatrix}$ , where the eigenvalues of the matrix correspond to the vibrational frequencies observed in Raman spectroscopy. Within this relation, the CDW amplitude mode softens as the temperature increases, gradually reaches zero frequency, and completely disappears around the CDW transition temperature  $T_{CDW}$ . The data points above the critical temperature  $T_{tr}$  are used for the fitting since the coupling with another peak around  $80\text{ cm}^{-1}$  is observed at a lower temperature, which causes a deviation from the coupling model of the two modes. The experimentally measured temperature dependence of the CDW modes has shown an excellent agreement with the Ginzburg–Landau equation as shown in Fig. 3(c). Based on the fittings,  $T_{CDW}$  is 378 K for GdTe<sub>3</sub> and 266 K for ErTe<sub>3</sub>. We note that these  $T_{CDW}$  values obtained from fitting were in close agreement with the values determined by macroscale electronic measurements as shown in Fig. 3(d).

Based on the close agreement seen in  $T_{CDW}$  values from electrical transport and Raman spectroscopy measurements, the  $T_{CDW}$  values were successfully determined for RTe<sub>3</sub> (R = Gd–Tm) by Raman spectroscopy. The CDW transition temperature decreased for increasing atomic number (increasing the number of 4f

electrons) as shown in Fig. 3(d) (red circles). This trend across the lanthanide series can be attributed to reduced lattice parameters or increased chemical pressure by heavier lanthanide atoms, in which the chemical pressure is qualitatively equivalent to the applied external pressure, reducing  $T_{CDW}$ . Figure 3(e) further shows that the extracted coupling constant  $\delta$  (Ginzburg–Landau fitting) increases for heavier lanthanide atoms (increased chemical pressure) while the critical exponent  $\beta$  value remains nearly constant. This finding implies that increasing the number of 4f electrons effectively increases the interaction between the CDW amplitude mode and phonon vibrational mode. Further theoretical studies are needed to clarify the origin of this effect.

#### Angle-resolved Raman spectroscopy and CDW transition.

The natural question arises as to how the symmetry of fundamental Raman modes changes as coupling with the amplitude mode takes place across the CDW transition. In our studies, we have performed angle-resolved Raman spectroscopy measurements on NdTe<sub>3</sub> and GdTe<sub>3</sub> above  $T_{CDW}$  and at the lowest attainable temperature (79 K) in our cryostat to elucidate these effects. The spectra of NdTe<sub>3</sub> and GdTe<sub>3</sub> at each temperature are shown in Fig. 4(a). The spectra above the CDW transition temperature are obtained at 500 K for NdTe<sub>3</sub> ( $T_{CDW} \sim 470$  K) and 380 K for GdTe<sub>3</sub> ( $T_{CDW} = 378$  K). The intensities of the phonon modes determined by Lorentz fitting under parallel polarization configuration are plotted with respect to the polarization angle Figs. 4(b) and 4(c) (the angle-resolved Raman spectra and the fittings are shown in the supplementary material). Here, the in-plane crystal structure orientation is determined by the angle-dependence of the CDW amplitude mode peak intensity.<sup>25</sup> The angle is defined as  $0^\circ$  when the polarization of the incident laser is along the *a*-lattice direction. Due to the weak Raman peak intensity and overlap with the CDW peak, fittings to the phonon mode at  $63\text{ cm}^{-1}$  for NdTe<sub>3</sub> (at 500 K) and  $114\text{ cm}^{-1}$  for GdTe<sub>3</sub> (at 79 K)

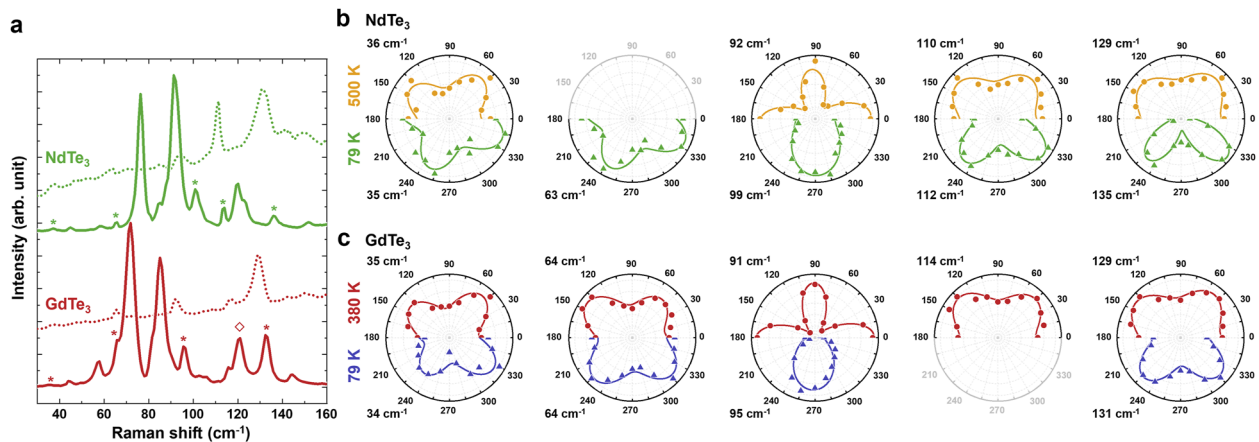


**FIG. 4.** (a) Raman spectra of NdTe<sub>3</sub> and GdTe<sub>3</sub> at 79 K (solid line) and above CDW transition temperature (dashed line). The spectra above the CDW transition temperature are obtained at 500 K for NdTe<sub>3</sub> and 380 K for GdTe<sub>3</sub>. Asterisks represent phonon modes related to the undistorted state. Angle dependence of phonon modes of (b) NdTe<sub>3</sub> and (c) GdTe<sub>3</sub> above (circles) and below (triangles) the CDW transition temperature. The fitting was not performed on the peak of NdTe<sub>3</sub> at 63 cm<sup>-1</sup> due to the small peak intensity. The peak of GdTe<sub>3</sub> at 114 cm<sup>-1</sup> overlapped with the CDW peak at 79 K (diamond).

were not possible [Fig. 4(b)]. Above the CDW transition temperature (at 500 K), all five Raman peaks show clear four-fold symmetry. The Raman modes at 35, 64, 114, and 129 cm<sup>-1</sup> maximize when the polarization vector is ~45° while that at 91 cm<sup>-1</sup> maximizes at ~90°, which indicates that the Raman mode at 91 cm<sup>-1</sup> and the other modes originate from the vibrational modes that have different symmetry. Below the transition temperature (79 K), the symmetry of the peaks at 35, 64, 114, and 129 cm<sup>-1</sup> remain the same, but the peak at 91 cm<sup>-1</sup> starts to display a two-lobed feature (it reaches a maximum at 90 and 270°). This polarization direction corresponds to the *c*-axis direction [Fig. 1(a)]. This result suggests that the distortion triggered by the CDW transition primarily affects the 91 cm<sup>-1</sup> peak and that this mode is involved in the coupling (phonon-electron and phonon-phonon) processes.

In summary, the results have introduced low-frequency temperature dependent Raman spectroscopy and angle-resolved Raman spectroscopy to access the CDW phase transition and related physical parameters in a wide range of lanthanide tritelluride materials. Findings have shown that the onset of the CDW transition,  $T_{\text{CDW}}$ , a CDW amplitude mode, can be observed in RTe<sub>3</sub> (R = Gd–Tm), and the temperature dependence of the CDW amplitude mode can be well-described by the Ginzburg–Landau model. The CDW transition temperature ( $T_{\text{CDW}}$ ) and other CDW-related parameters can be well determined after fitting into the Ginzburg–Landau model. Angle-resolved Raman studies highlighted which Raman modes undergo significant symmetry changes across the CDW transition temperature. Findings introduce complete Raman spectroscopy studies on RTe<sub>3</sub> CDW materials and extend the knowledge in these unique material systems.

## SUPPLEMENTARY MATERIAL

See the [supplementary material](#) for the growth condition, the complete sets of temperature dependent Raman spectra, and the details of the Lorentz fitting.

## ACKNOWLEDGMENTS

S.T. acknowledges support from Applied Materials Inc., under Grant Nos. DOE-SC0020653, NSF CMMI 1825594, NSF DMR-1955889, NSF CMMI-1933214, NSF 1904716, NSF 1935994, NSF ECCS 2052527, and DMR 2111812.

## AUTHOR DECLARATIONS

### Conflict of Interest

The authors have no conflicts to disclose.

### Author Contributions

K.Y. contributed to this paper.

**Kentaro Yumigeta:** Data curation (lead); Formal analysis (lead); Investigation (lead); Methodology (equal); Resources (equal); Visualization (lead); Writing—original draft (lead). **Yashika Attarde:** Data curation (equal); Formal analysis (supporting); Investigation (equal); Methodology (equal); Resources (equal); Validation (equal); Visualization (supporting); Writing—review & editing (supporting). **Jan Kopaczek:** Investigation (supporting); Validation (supporting); Writing—review & editing (supporting). **Mohammed Y. Sanyad:** Investigation (supporting); Validation (supporting). **Yuxia Shen:** Resources (equal). **Mark Blei:** Resources (equal). **Ying Qin:** Resources (equal). **Renee Sailus:** Investigation (supporting); Validation (equal). **Sefaattin Tongay:** Conceptualization (lead); Funding acquisition (lead); Project administration (lead); Supervision (lead); Visualization (supporting); Writing—review & editing (lead).

## DATA AVAILABILITY

The data that support the findings of this study are available within the article and its [supplementary material](#).

## REFERENCES

- <sup>1</sup>S. Lei, J. Lin, Y. Jia, M. Gray, A. Topp, G. Farahi, S. Klemenz, T. Gao, F. Rodolakis, J. L. McChesney, C. R. Ast, A. Yazdani, K. S. Burch, S. Wu, N. P. Ong, and L. M. Schoop, "High mobility in a van der Waals layered antiferromagnetic metal," *Sci Adv* **6**(6), eaay6407 (2020).
- <sup>2</sup>J. J. Hamlin, D. A. Zocco, T. A. Sayles, M. B. Maple, J. H. Chu, and I. R. Fisher, "Pressure-induced superconducting phase in the charge-density-wave compound terbium tritelluride," *Phys. Rev. Lett.* **102**(17), 177002 (2009).
- <sup>3</sup>D. A. Zocco, J. J. Hamlin, K. Grube, J. H. Chu, H. H. Kuo, I. R. Fisher, and M. B. Maple, "Pressure dependence of the charge-density-wave and superconducting states in GdTe<sub>3</sub>, TbTe<sub>3</sub>, and DyTe<sub>3</sub>," *Phys. Rev. B* **91**(20), 205114 (2015).
- <sup>4</sup>M. Watanabe, R. Nakamura, S. Lee, T. Asano, T. Ibe, M. Tokuda, H. Taniguchi, D. Ueta, Y. Okada, K. Kobayashi, and Y. Niimi, "Shubnikov-de-Haas oscillation and possible modification of effective mass in CeTe<sub>3</sub> thin films," *AIP Adv.* **11**(1), 015005 (2021).
- <sup>5</sup>Z. Yang, A. J. Drew, S. van Smaalen, N. van Well, F. L. Pratt, G. B. G. Stenning, A. Karim, and K. Rabia, "Multiple magnetic-phase transitions and critical behavior of charge-density wave compound TbTe<sub>3</sub>," *J. Phys.: Condens. Matter* **32**(30), 305801 (2020).
- <sup>6</sup>J. Yin, C. Wu, L. Li, J. Yu, H. Sun, B. Shen, B. A. Frandsen, D.-X. Yao, and M. Wang, "Large negative magnetoresistance in the antiferromagnetic rare-earth dichalcogenide EuTe<sub>2</sub>," *Phys. Rev. Mater.* **4**(1), 013405 (2020).
- <sup>7</sup>M. Watanabe, S. Lee, T. Asano, T. Ibe, M. Tokuda, H. Taniguchi, D. Ueta, Y. Okada, K. Kobayashi, and Y. Niimi, "Quantum oscillations with magnetic hysteresis observed in CeTe<sub>3</sub> thin films," *Appl. Phys. Lett.* **117**(7), 072403 (2020).
- <sup>8</sup>P. Walmsley, S. Aeschlimann, J. A. W. Straquadine, P. Giraldo-Gallo, S. C. Riggs, M. K. Chan, R. D. McDonald, and I. R. Fisher, "Magnetic breakdown and charge density wave formation: A quantum oscillation study of the rare-earth tritellurides," *Phys. Rev. B* **102**(4), 045150 (2020).
- <sup>9</sup>J. A. W. Straquadine, M. S. Ikeda, and I. R. Fisher, "Evidence for realignment of the charge density wave state in ErTe<sub>3</sub> and TmTe<sub>3</sub> under uniaxial stress via elastocaloric and elastoresistivity measurements," *Phys. Rev. X* **12**(2), 021046 (2022).
- <sup>10</sup>R. Okuma, D. Ueta, S. Kuniyoshi, Y. Fujisawa, B. Smith, C. H. Hsu, Y. Inagaki, W. Si, T. Kawae, H. Lin, F. C. Chuang, T. Masuda, R. Kobayashi, and Y. Okada, "Fermionic order by disorder in a van der Waals antiferromagnet," *Sci. Rep.* **10**(1), 15311 (2020).
- <sup>11</sup>A. Pariari, S. Koley, S. Roy, R. Singha, M. S. Laad, A. Taraphder, and P. Mandal, "Interplay between charge density wave order and magnetic field in the nonmagnetic rare-earth tritelluride LaTe<sub>3</sub>," *Phys. Rev. B* **104**, 155147 (2021).
- <sup>12</sup>A. Kogar, A. Zong, P. E. Dolgirev, X. Shen, J. Straquadine, Y.-Q. Bie, X. Wang, T. Rohwer, I.-C. Tung, Y. Yang, R. Li, J. Yang, S. Weathersby, S. Park, M. E. Kozina, E. J. Sie, H. Wen, P. Jarillo-Herrero, I. R. Fisher, X. Wang, and N. Gedik, "Light-induced charge density wave in LaTe<sub>3</sub>," *Nat. Phys.* **16**(2), 159–163 (2019).
- <sup>13</sup>F. Zhou, J. Williams, S. Sun, C. D. Malliakas, M. G. Kanatzidis, A. F. Kemper, and C.-Y. Ruan, "Nonequilibrium dynamics of spontaneous symmetry breaking into a hidden state of charge-density wave," *Nat. Commun.* **12**(1), 566 (2021).
- <sup>14</sup>A. A. Sinchenko, P. D. Grigoriev, P. Lejay, and P. Monceau, "Linear magnetoresistance in the charge density wave state of quasi-two-dimensional rare-earth tritellurides," *Phys. Rev. B* **96**(24), 245129 (2017).
- <sup>15</sup>N. Ru, C. L. Condrón, G. Y. Margulis, K. Y. Shin, J. Laverock, S. B. Dugdale, M. F. Toney, and I. R. Fisher, "Effect of chemical pressure on the charge density wave transition in rare-earth tritellurides RTe<sub>3</sub>," *Phys. Rev. B* **77**(3), 035114 (2008).
- <sup>16</sup>J. F. Cannon and H. T. Hall, "High-pressure, high-temperature syntheses of selected lanthanide-tellurium compounds," *Inorg. Chem.* **9**(7), 1639–1643 (1970).
- <sup>17</sup>C. D. Malliakas and M. G. Kanatzidis, "Divergence in the behavior of the charge density wave in RETe<sub>3</sub> (RE = rare-earth element) with temperature and RE element," *J. Am. Chem. Soc.* **128**(39), 12612–12613 (2006).
- <sup>18</sup>N. Ru, J. H. Chu, and I. R. Fisher, "Magnetic properties of the charge density wave compounds RTe<sub>3</sub> (R = Y, La, Ce, Pr, Nd, Sm, Gd, Tb, Dy, Ho, Er, and Tm)," *Phys. Rev. B* **78**(1), 012410 (2008).
- <sup>19</sup>E. DiMasi, M. C. Aronson, J. F. Mansfield, B. Foran, and S. Lee, "Chemical pressure and charge-density waves in rare-earth tritellurides," *Phys. Rev. B* **52**(20), 14516–14525 (1995).
- <sup>20</sup>N. Ru, *Charge Density Wave Formation in Rare-Earth Tritellurides* (Stanford University, 2008).
- <sup>21</sup>A. Banerjee, Y. Feng, D. M. Silevitch, J. Wang, J. C. Lang, H. H. Kuo, I. R. Fisher, and T. F. Rosenbaum, "Charge transfer and multiple density waves in the rare earth tellurides," *Phys. Rev. B* **87**(15), 155131 (2013).
- <sup>22</sup>M. Lavagnini, H. M. Eiter, L. Tassini, B. Muschler, R. Hackl, R. Monnier, J. H. Chu, I. R. Fisher, and L. Degiorgi, "Raman scattering evidence for a cascade evolution of the charge-density-wave collective amplitude mode," *Phys. Rev. B* **81**(8), 081101 (2010).
- <sup>23</sup>Y. Chen, P. Wang, M. Wu, J. Ma, S. Wen, X. Wu, G. Li, Y. Zhao, K. Wang, L. Zhang, L. Huang, W. Li, and M. Huang, "Raman spectra and dimensional effect on the charge density wave transition in GdTe<sub>3</sub>," *Appl. Phys. Lett.* **115**(15), 151905 (2019).
- <sup>24</sup>N. Lazarević, Z. V. Popović, R. Hu, and C. Petrovic, "Evidence of coupling between phonons and charge-density waves in ErTe<sub>3</sub>," *Phys. Rev. B* **83**(2), 024302 (2011).
- <sup>25</sup>H.-M. Eiter, M. Lavagnini, R. Hackl, E. A. Nowadnick, A. F. Kemper, T. P. Devereaux, J.-H. Chu, J. G. Analytis, I. R. Fisher, and L. Degiorgi, "Alternative route to charge density wave formation in multiband systems," *Proc. Natl. Acad. Sci. U. S. A.* **110**(1), 64–69 (2013).
- <sup>26</sup>J. S. Liu, S. C. Huan, Z. H. Liu, W. L. Liu, Z. T. Liu, X. L. Lu, Z. Huang, Z. C. Jiang, X. Wang, N. Yu, Z. Q. Zou, Y. F. Guo, and D. W. Shen, "Electronic structure of the high-mobility two-dimensional antiferromagnetic metal GdTe<sub>3</sub>," *Phys. Rev. Mater.* **4**(11), 114005 (2020).
- <sup>27</sup>G. Wang, E. Palleau, T. Amand, S. Tongay, X. Marie, and B. Urbaszek, "Polarization and time-resolved photoluminescence spectroscopy of excitons in MoSe<sub>2</sub> monolayers," *Appl. Phys. Lett.* **106**(11), 112101 (2015).
- <sup>28</sup>R. Beams, L. G. Cançado, S. Krylyuk, I. Kalish, B. Kalanyan, A. K. Singh, K. Choudhary, A. Bruma, P. M. Vora, F. Tavazza, A. V. Davydov, and S. J. Stranick, "Characterization of few-layer 1T' MoTe<sub>2</sub> by polarization-resolved second harmonic generation and Raman scattering," *ACS Nano* **10**(10), 9626–9636 (2016).
- <sup>29</sup>K. Wu, B. Chen, S. Yang, G. Wang, W. Kong, H. Cai, T. Aoki, E. Soignard, X. Marie, A. Yano, A. Sulus, B. Urbaszek, and S. Tongay, "Domain architectures and grain boundaries in chemical vapor deposited highly anisotropic ReS<sub>2</sub> monolayer films," *Nano Lett.* **16**(9), 5888–5894 (2016).
- <sup>30</sup>W. Kong, C. Bacaksiz, B. Chen, K. Wu, M. Blei, X. Fan, Y. Shen, H. Sahin, D. Wright, D. S. Narang, and S. Tongay, "Angle resolved vibrational properties of anisotropic transition metal trichalcogenide nanosheets," *Nanoscale* **9**(12), 4175–4182 (2017).
- <sup>31</sup>W. Wen, Y. Zhu, X. Liu, H. P. Hsu, Z. Fei, Y. Chen, X. Wang, M. Zhang, K. H. Lin, F. S. Huang, Y. P. Wang, Y. S. Huang, C. H. Ho, P. H. Tan, C. Jin, and L. Xie, "Anisotropic spectroscopy and electrical properties of 2D ReS<sub>2</sub>(1-x)Se<sub>2x</sub> alloys with distorted 1T structure," *Small* **13**(12), 1603788 (2017).
- <sup>32</sup>B. Aslan, D. A. Chenet, A. M. van der Zande, J. C. Hone, and T. F. Heinz, "Linearly polarized excitons in single- and few-layer ReS<sub>2</sub> crystals," *ACS Photonics* **3**(1), 96–101 (2015).
- <sup>33</sup>A. Pant, E. Torun, B. Chen, S. Bhat, X. Fan, K. Wu, D. P. Wright, F. M. Peeters, E. Soignard, H. Sahin, and S. Tongay, "Strong dichroic emission in the pseudo one dimensional material ZrS<sub>3</sub>," *Nanoscale* **8**(36), 16259–16265 (2016).
- <sup>34</sup>K. Wu, E. Torun, H. Sahin, B. Chen, X. Fan, A. Pant, D. Parsons Wright, T. Aoki, F. M. Peeters, E. Soignard, and S. Tongay, "Unusual lattice vibration characteristics in whiskers of the pseudo-one-dimensional titanium trisulfide TiS<sub>3</sub>," *Nat. Commun.* **7**, 12952 (2016).
- <sup>35</sup>W. Zhu, L. Liang, R. H. Roberts, J.-F. Lin, and D. Akinwande, "Anisotropic electron-phonon interactions in angle-resolved Raman study of strained black phosphorus," *ACS Nano* **12**(12), 12512–12522 (2018).
- <sup>36</sup>K. Wu, M. Blei, B. Chen, L. Liu, H. Cai, C. Brayfield, D. Wright, H. Zhuang, and S. Tongay, "Phase transition across anisotropic NbS<sub>3</sub> and direct gap semiconductor TiS<sub>3</sub> at nominal titanium alloying limit," *Adv. Mater.* **32**(17), e2000018 (2020).

- <sup>37</sup>J. Qin, G. Qiu, J. Jian, H. Zhou, L. Yang, A. Charnas, D. Y. Zemlyanov, C.-Y. Xu, X. Xu, W. Wu, H. Wang, and P. D. Ye, "Controlled growth of a large-size 2D selenium nanosheet and its electronic and optoelectronic applications," *ACS Nano* **11**(10), 10222–10229 (2017).
- <sup>38</sup>Y. Liu, Q. Gu, Y. Peng, S. Qi, N. Zhang, Y. Zhang, X. Ma, R. Zhu, L. Tong, J. Feng, Z. Liu, and J. H. Chen, "Raman signatures of broken inversion symmetry and in-plane anisotropy in type-II Weyl semimetal candidate TaIrTe<sub>4</sub>," *Adv. Mater.* **30**(25), e1706402 (2018).
- <sup>39</sup>H. M. Hill, S. Chowdhury, J. R. Simpson, A. F. Rigosi, D. B. Newell, H. Berger, F. Tavazza, and A. R. H. Walker, "Phonon origin and lattice evolution in charge density wave states," *Phys. Rev. B* **99**, 174110 (2019).
- <sup>40</sup>D. Lin, S. Li, J. Wen, H. Berger, L. Forró, H. Zhou, S. Jia, T. Taniguchi, K. Watanabe, X. Xi, and M. S. Bahrany, "Patterns and driving forces of dimensionality-dependent charge density waves in 2H-type transition metal dichalcogenides," *Nat. Commun.* **11**(1), 2406 (2020).
- <sup>41</sup>L. Cui, R. He, G. Li, Y. Zhang, Y. You, and M. Huang, "Raman spectroscopy of optical phonon and charge density wave modes in 1T-TiSe<sub>2</sub> exfoliated flakes," *Solid State Commun.* **266**, 21–25 (2017).
- <sup>42</sup>R. V. Yusupov, T. Mertelj, J.-H. Chu, I. R. Fisher, and D. Mihailovic, "Single-particle and collective mode couplings associated with 1- and 2-directional electronic ordering in metallic RTe<sub>3</sub> (R = Ho, Dy, Tb)," *Phys. Rev. Lett.* **101**(24), 246402 (2008).
- <sup>43</sup>G. Grüner, *Density Waves in Solids* (CRC Press, 2018).